38th Fluid Dynamics Conference and Exhibit
23 - 26 June 2008, Seattle, Washington

AIAA 2008-4177

Coupled CFD and Particle Vortex Transport Method: Wing Performance and Wake Validations

Phuriwat Anusonti-Inthra[1]
National Institute of Aerospace, Hampton, Virginia, 23666, USA

Matt Floros[2]
US Army Research Laboratory, Hampton, Virginia, 23681, USA

The development of a new hybrid CFD approach using fully coupled Reynolds-Averaged Navier-Stokes (RANS) and Particle-based Vorticity Transport Method (PVTM) solvers is summarized in this paper. The methodology is applied to predict the performance and wake parameters of an isolated wing in low speed flow condition. The approach divides the flow field into several regions and uses appropriate flow solvers according to the dominant physical features of the flow in each region. The near body flow field, which is dominated by the effect of viscosity and geometry, is resolved using a 3D compressible RANS solver. The flow field outside of the RANS regions, which is primarily dominated by the vortices being shed from the aerodynamic surfaces, is simulated using a viscous implementation of the Particle-based Vorticity Transport Method. The coupling methodology and the appropriate information being transferred between the two solvers are also outlined. A stability enhancement procedure is implemented for the PVTM analysis. The results obtained using the coupled RANS/PVTM analysis compare well with experimental data, in particular the pressure distribution, sectional load, and tip vortex parameters (swirl velocity, core location, and core size).

Nomenclature

α, β, Γ	=	strength of vortex particle ($\int \omega dV$)
ϕ	=	vortex core function
ρ	=	density
ν	=	kinematic viscosity
ω	=	vorticity vector
A	=	differential area of outer boundary
c	=	wing chord
C_L	=	lift force coefficient
C_D	=	drag force coefficient
$dt, \Delta t$	=	time step
dV	=	differential Volume
dx	=	differential distance from vortex particle
f_{ij}	=	vortex splitting coefficients
$\hat{n}$	=	outward normal vector
P	=	pressure
u,V	=	velocity vector
Re	=	Reynolds number
R	=	wing span
S	=	vorticity Source
t	=	time
X	=	location vector

[1]Senior Research Scientist, 100 Exploration Way
[2] Aerospace Engineer, Vehicle Technology Directorate, NASA Langley Research Center MS 266, AIAA member

Report Documentation Page

Form Approved
OMB No. 0704-0188

1. REPORT DATE	2. REPORT TYPE	3. DATES COVERED
JUN 2008		**00-00-2008 to 00-00-2008**

4. TITLE AND SUBTITLE	5a. CONTRACT NUMBER
Coupled CFD and Particle Vortex Transport Method: Wing Performance and Wake Validations	5b. GRANT NUMBER
	5c. PROGRAM ELEMENT NUMBER
6. AUTHOR(S)	5d. PROJECT NUMBER
	5e. TASK NUMBER
	5f. WORK UNIT NUMBER
7. PERFORMING ORGANIZATION NAME(S) AND ADDRESS(ES) **US Army Research Laboratory,Hampton,VA,23681**	8. PERFORMING ORGANIZATION REPORT NUMBER
9. SPONSORING/MONITORING AGENCY NAME(S) AND ADDRESS(ES)	10. SPONSOR/MONITOR'S ACRONYM(S)
	11. SPONSOR/MONITOR'S REPORT NUMBER(S)

12. DISTRIBUTION/AVAILABILITY STATEMENT
Approved for public release; distribution unlimited

13. SUPPLEMENTARY NOTES

14. ABSTRACT

15. SUBJECT TERMS

16. SECURITY CLASSIFICATION OF:			17. LIMITATION OF ABSTRACT	18. NUMBER OF PAGES	19a. NAME OF RESPONSIBLE PERSON
a. REPORT **unclassified**	b. ABSTRACT **unclassified**	c. THIS PAGE **unclassified**	**Same as Report (SAR)**	**12**	

I. Introduction

Accurately predicting the long-term dynamics of the wake produced by a wing under high Reynolds number flow conditions is still one of the most challenging tasks for CFD simulations. In the simplest form, the wake behind a wing in these flow conditions usually consists of vortex sheet from the boundary layer and a strong tip vortex from 3D finite wing effects. The tip vortex is quickly formed and is normally well organized before leaving the wing trailing edge[1]. A typical velocity profile of the tip vortex can be found in Ref. 2. The tip vortex continues strengthening after leaving the trailing edge by rolling in the vortex sheet. Then the viscous diffusion effect causes the tip vortex to grow in size and lose strength very slowly as it convects downstream. The wake behind a real aircraft is much more complex[3]. Normally, tip vortices can stay coherent for some distance behind the wing, and the lifespan of the tip vortices is highly dependent on atmospheric conditions[4]. After that the tip vortices can start interacting with other vortices and cause wake instability[5] that has been observed in flight tests[6]. This instability is very complex phenomenon[7], and involves the merging of unequal strength counter-rotating vortex pairs[8]. The simulations of such complex flow conditions, however, are beyond the scope of this paper.

Many researchers have successfully been simulating such wake flow using increasingly complicated approaches. The earliest attempts simplified the wake structure and modeled it using a vortex filament method[9] or vortex panel method[10]. A classical wing theory has also been modified to simulate the wake behind a wing[11]. Recently, various Computational Fluid Dynamics (CFD) methods have been used commonly to calculate such flow, and in one such study, two CFD solvers (RANS and hybrid Euler/LES solvers) were used to compute aircraft wakes very far downstream, with an equivalent distance of 2.89 nautical miles for a full scale Airbus A340[12]. In addition, vortex particle methods have been used to simulate high resolution wake from aircraft using billions of particles[13].

Conventional CFD calculations can simulate the generation and evolution of the vortex sheet and tip vortex well if sufficient numbers of grid points are used to resolve those flow features. These calculations require localized refinement near high velocity gradient regions such as the leading and trailing edges, boundary layer, vortex sheet, and tip vortices). High-order CFD algorithms can also be used to improve the accuracy of the calculation in the high gradient regions. Even with the grid refinement and high-order CFD algorithms, the conventional CFD simulations still suffer from excessive numerical dissipation, which typically causes the tip vortex to diffuse prematurely. This numerical diffusion often causes the tip vortex core size to grow faster than it should based on physics. Though the core size becomes large, the vortex strength is preserved, which may be adequate for many applications. However, for certain specific applications like noise and vibration calculations or wake interactions, accurate predictions of the vortex core size and velocity profile are very important.

Recently, a new hybrid approach using fully coupled Reynolds-Averaged Navier-Stokes (RANS) and Particle-based Vorticity Transport Method (PVTM) solvers was introduced to simulate rotorcraft wake flow[14]. The approach divides the flow field into several regions and uses appropriate flow solvers according to the dominant physical features of the flow in each region. The first region covers the flow field near aerodynamic surfaces (extending about 1 chord from the surfaces), where the flow features are dominated by the effects of boundary layer viscosity and the geometry of the airfoil and blade planform. The near body flow field is resolved using a 3D compressible RANS solver[15]. Outside of the RANS regions, the flow field is primarily dominated by the vortices being shed from the aerodynamic surfaces. This vortex-dominated flow region is simulated using a Particle-based Vorticity Transport Method (PVTM). The influence of this far field flow region is transferred to the RANS regions using the field velocity approach[15]. By modeling the far field with PVTM, the shed vorticity can remain well organized and in particular the tip vortices can maintain their compact and stable cores for a longer period of time than vortices simulated using conventional RANS/CFD. This approach is particularly suitable for rotorcraft applications where maintaining the correct velocity gradient in the vortex core is critical for acoustic and vibratory loads calculations, which depend greatly on the location, size, and strength of the vortex. A previous study showed that the methodology is viable, but did not illustrate quantitatively how well the approach predicted the near body flow field and associated vortex-dominated flow field[14].

II. Focus of the Present study

In the present study, the coupled RANS/PVTM method is validated against wind tunnel test data. Comparisons with measured pressure distribution, loadings, and vortex parameters, and the corresponding results from the full RANS and coupled RANS/PVTM simulations are presented for a semi-span NACA 0015 wing. The objectives are to verify that the coupled approach accurately models the wake and properly maintains the tip vortex geometry. Although RANS calculations are provided for reference, the pure RANS calculations do not take advantage of

higher order or refinement techniques, so they do not represent the state of the art in wake modeling with RANS CFD. Rather, they represent a baseline to gauge the effectiveness of an alternative method to grid refinement.

III. Approach and Method

The conventional RANS and coupled RANS/PVTM analyses are used to calculate the wing performance and wake parameters for comparison with experimental data. The results from the first approach which simulates the entire flow field using only RANS calculation are used as a baseline. This baseline is compared to the results obtained using the hybrid RANS/PVTM approach which simulates the flow in the near and far fields separately using RANS and PVTM, respectively. The following sections describe computational setup and summarize the development of the coupled RANS/PVTM methodology.

A. Modeling Experimental Test Conditions

A comprehensive experiment to measure the detailed progression of the tip vortex from a semi-span NACA 0015 wing[16], conducted at the NASA Ames 7- by 10-Foot Subsonic Wind Tunnel, is used as the reference data to validate the results from the RANS/PVTM simulations. The experiment used a pressure-instrumented, untwisted semi-span NACA 0015 wing with a square tip (meaning the end is flat and perpendicular to the span axis). A round end cap was installed for some conditions to change the tip geometry of the wing from square tip to rounded tip. The experiments were conducted for a small range of Reynolds numbers between 1×10^6 and 3×10^6. Velocity profiles across the tip vortex were measured at various downstream locations up to 6 chords behind the wing using a two-component laser velocimeter. The data provided by this test include *(i)* the chordwise pressure distribution along several span locations; *(ii)* the velocity, location, and core size of the tip vortex; *(iii)* integrated sectional lift, drag, and moment coefficients at various span locations.

The experimental configuration and condition described in Ref. 16 is used to develop computational models of the semi-span NACA 0015 wing. The rectangular wing has a constant and untwisted NACA 0015 profile along the span with a full-span aspect ratio of 6.6. The wing was mounted on a vertical supporting end plate that fitted 1 foot away from the side wall of the tunnel. This end plate prevents the formation of the trailing vortex near the mounting point and effectively creates an infinite wing (2D) boundary condition at the mounting point. Several angles of attack were tested in the experiment. For the current study, only one angle of attack of 12° is simulated. An additional 0.51° is added to the angle of attack in the simulations as a correction for the closed-tunnel wall effect[16]. The free-stream velocity corresponds to a Mach number of 0.13 and Reynolds number of $1.5\text{x}10^6$.

B. Full Reynolds-Averaged Navier-Stokes (RANS) Analysis

The baseline or full RANS simulation results in the present study are obtained using the TURNS 3D compressible solver[15]. The analysis solves the RANS equations for primitive variables ρ, ρV, ρE inside a 3D structured grid using a finite volume approach. The grid used in the calculation for the square tip wing is presented in Figure 1 with the dimension of $399\times131\times97$ grid points. The grid extends to about 6 chords in all directions from the wing surface, and grid points are distributed a priori and mostly concentrated in regions with high velocity gradient such as near the leading edge, boundary layer, tip vortex, and vortex sheet. The boundary condition at the root of the wing is set to be extrapolated from flow parameters inside the RANS domain, simulating the infinite wing (2D) boundary condition to match the experiment.

C. Coupled RANS/Particle-based Vorticity Transport Method

In the coupled RANS/PVTM analysis[14], the flow field is divided into a near-body grid and a far field region. The flow field in the near-body grid is solved using the same 3D compressible RANS solver and boundary conditions described in the previous section, but the domain is much smaller. The RANS domain extends to about 1 chord length in all directions except behind the trailing edge, where it extends only to about 0.5 chord length, see Figure 2. The small extent behind the trailing edge minimizes the dissipation of vorticity to be transferred into PVTM domain. This small RANS grid has a dimension of $249\times131\times79$ grid points. The same 2D boundary condition at the wing root is used. In addition, the induced velocity from the vortex particles in the far field is included in the RANS calculation as field velocity[15].

Outside the near body RANS domain, the flow field is represented by collections of three-dimensional vortex particles similar to those presented in Ref. 17. Each vortex particle has two vector quantities, namely location and strength, associated with it. The strength of the vortex is a volume integration of the vorticity field around the particle, and the evolution of the strength is governed by the vorticity transport equations:

$$\int \frac{d\omega}{dt} dV_i = \int [\omega \cdot \nabla u] dV_i + \int [\nu \nabla^2 \omega] dV_i + S_i \tag{1}$$

where u is the local velocity, ω is vorticity, ν is kinematic viscosity, and S_i is the vorticity source inside a differential volume dV_i. The derivation of the vorticity source will be explained in a separate section below. The location of the particle is changed due to local velocity induced by other vortex particles in the flow field. The detailed derivation and implementation of the PVTM analysis can be found in Ref. 14, and is briefly summarized below.

For convenience in the PVTM domain, a multi-level background Cartesian coordinate system shown in Figure 3 is used to facilitate fundamental vortex particle operations such as volume integration, tracking, merging, splitting, and induced velocity calculation. The PVTM coordinate system is different than a grid system in that no variables are being solved at grid points. Its purpose is for numerical integration and for tracking of vortex particles. The coordinate system has fine ($0.05c$) and coarse ($0.2c$) levels which extend to $8c$ and $20c$ behind the wing, respectively. To reduce computational cost, only one particle is allowed in each cell. If two or more particles move into the same cell they are merged with the new strength being the sum of the strength of the merged particles, and the new location being the strength-weighted centroid of the particles. The induced velocity is calculated using the Biot-Savart law, and the vortex stretching term, $\omega \cdot \nabla u$, is calculated by differentiating the velocity field. The multi-level particle mesh approach is employed to reduce computational effort for calculating the induced velocity and stretching term.

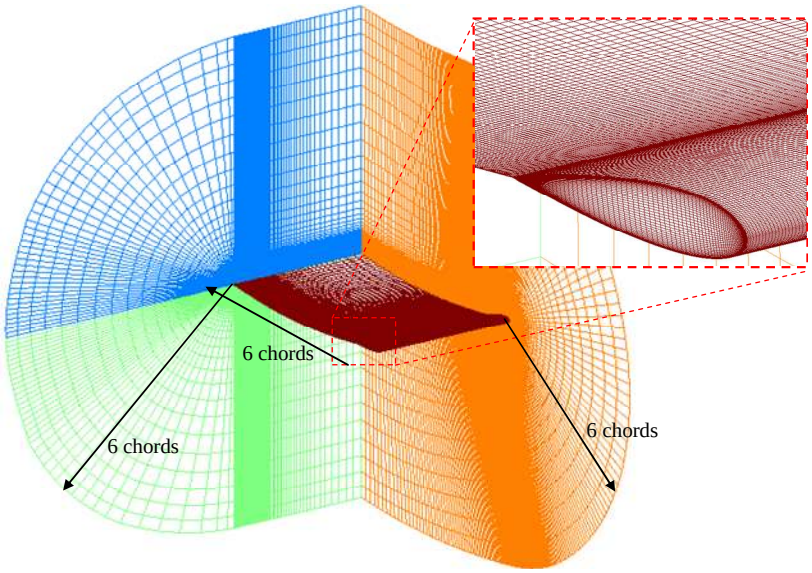

Figure 1. Grid for full RANS calculation of the square tip wing (5M grid points).

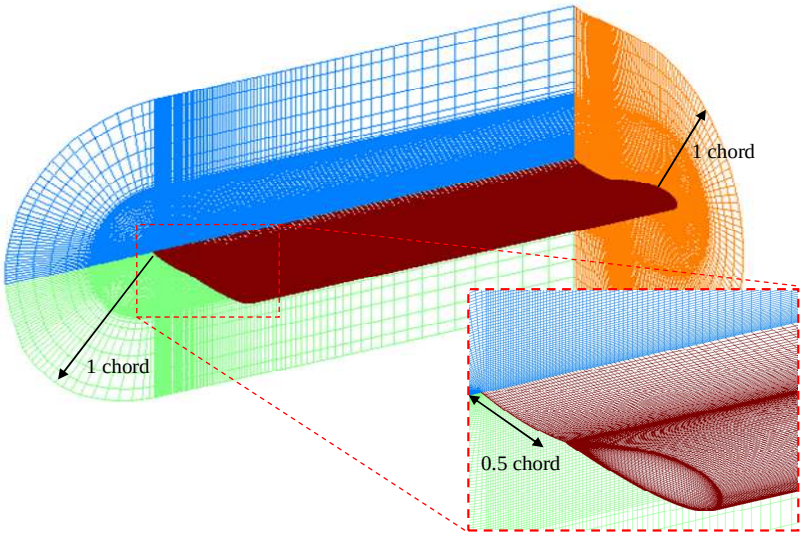

Figure 2. Grid for coupled RANS/PVTM calculation of the square tip wing (2.5M grid points).

The vorticity source for the PVTM domain is derived from the convection of the vorticity field from the boundary of the RANS domain. For each RANS cell that is on the boundary, the vorticity convected from the RANS domain to the PVTM domain is defined as follows:

$$\alpha_r = \int \omega A \cdot (u \cdot \hat{n}) dt \tag{2}$$

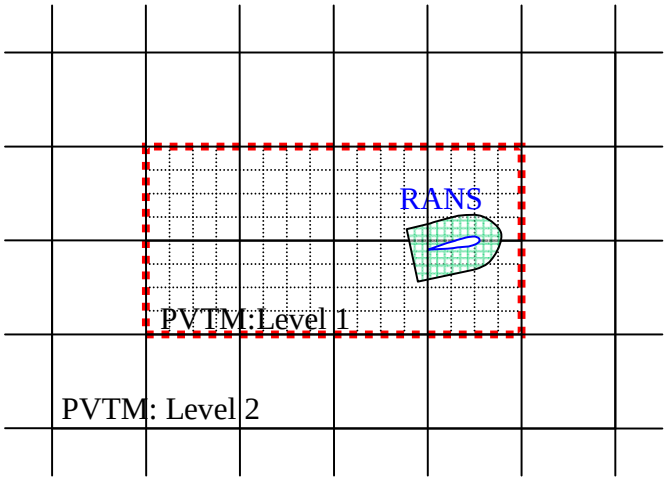

Figure 3. A 2D view of a representative 3D multi-level background grid for PVTM domain.

where α_r is the strength of the released particle, X_r is the location of the released particle, A is area of the outer boundary, $\hat{n}$ is outward normal vector and X_{mid} is the mid-point of the area A.

The viscous diffusion effect is simulated using the vorticity redistribution method[18,19], which is performed separately from the particle convection step. In this study, a single vortex particle is split into five smaller particles in the diffusion step. The locations of the five particles are defined by the vertices of a randomly oriented tetrahedron and its center (see Figure 4). The number and locations of the diffused particles are somewhat arbitrary, and they are chosen this way to maintain the symmetry of the vorticity field. The strengths of the particles are determined by a series expansion that preserves vorticity and its moments (i.e. $\int \omega$, $\int \omega x dx$, and $\int \omega x^2 dx$). The diffusion equations are summarized in Eq. (3) in non-dimensionalized form.

$$\frac{\partial \omega}{\partial t} = \frac{1}{\mathrm{Re}} \nabla^2 \omega \tag{3}$$

$$\omega_i(x, t + \Delta t_d) = \sum_{j=1}^{5} f_{ij} \Gamma_i \phi(\hat{x}_{ij})$$

where $\hat{x}_{ij} = (x_j - x_i)/h$, $h = \sqrt{\Delta t_d}$, Re: Reynolds number, f_{ij} are determined by series expansion such that $\sum_j f_{ij} = 1, \sum_j f_{ij}\hat{x}_{ij} = \sum_j f_{ij}\hat{y}_{ij} = \sum_j f_{ij}\hat{z}_{ij} = 0, \sum_j f_{ij}\hat{x}_{ij}\hat{y}_{ij} = \sum_j f_{ij}\hat{y}_{ij}\hat{z}_{ij} = \sum_j f_{ij}\hat{x}_{ij}\hat{z}_{ij} = 0, \sum_j f_{ij}\hat{x}_{ij}^2 = \sum_j f_{ij}\hat{y}_{ij}^2 = \sum_j f_{ij}\hat{z}_{ij}^2 = 2$,

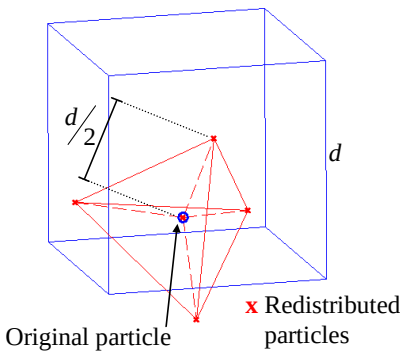

Figure 4. Schematic of vorticity redistribution scheme.

$\Gamma_i = \int \omega dV_i$, ϕ is the vortex core function, and $\Delta t_d = N\Delta t$. Due to the high Reynolds number flow condition, the diffusion step is performed at every N time steps to increase the effective diffusion distance, h, and avoid canceling this diffusion effect with the merging of the particles.

The process in which each vortex particle, $\beta_i = \int \omega dV_i$, is created, changed, and evolved with time is simulated by a two-step procedure. The first step is a convection step which is performed at every time step and is summarized in Eqs. (4). Equations (4) are solved using 4th order Runge-Kutta time integration algorithm with an adaptive time stepping procedure, which appropriately adjusts the time step size (dt) based on local velocity and stress fields to maintain desired computational accuracy.

$$\beta_i^k = \beta_i^{k-1} + \int \left(\beta_i^{k-1} \cdot \nabla u\right) dt + \alpha_r \tag{4}$$

$$x_i^k = x_i^{k-1} + \int u dt$$

The source term, α_r, is calculated from Eq. (2). The superscripts (*k*, *k-1*) are the time step indices, and the subscripts (*i*) are particle number indices. The second diffusion step is performed at every *N* time steps and the governing equation is given in Eq. (5).

$$\beta_i^k = \sum_j f_{ij} \beta_i^{k-1} \tag{5}$$

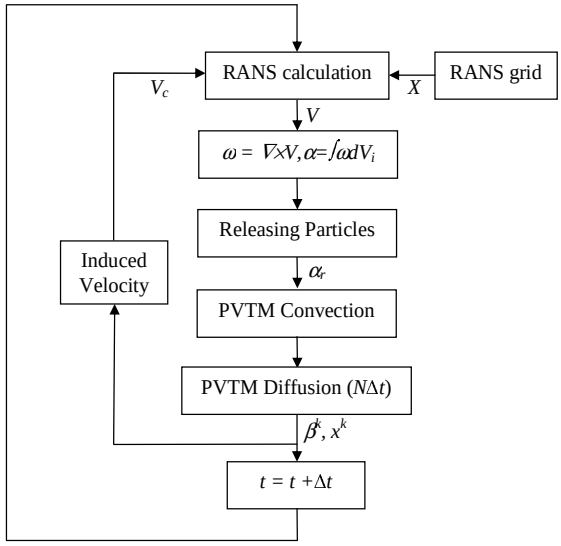

Figure 5 Coupling procedure for fully coupled RANS/PVTM analysis.

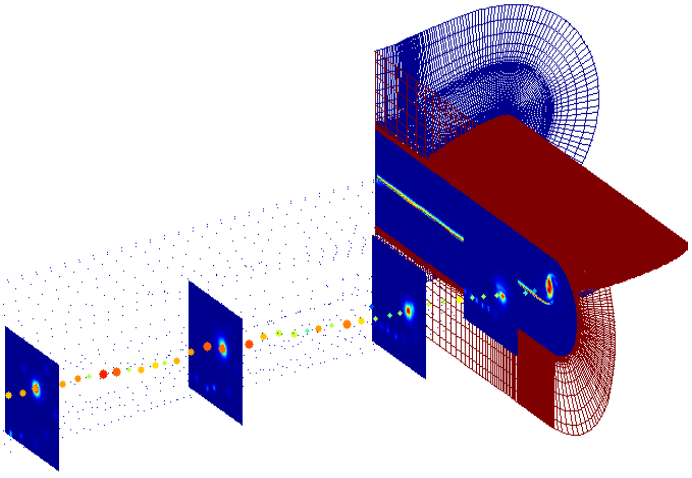

Figure 6. Vorticity profile calculated using coupled RANS/PVTM method showing velocity planes and vortex particles in trailed wake.

A flowchart describing the coupling procedure between RANS and PVTM is shown in Figure 5. At the start of any time step, the RANS calculation is performed to obtain flow parameters that include the induced velocity from far-field vortex particles as field velocity. After the RANS calculation is completed, the velocity field in the RANS domain is transformed into vorticity field, and vortex particles are released into the PVTM domain using Eq. (2). Then these newly released particles are added to the existing particles in the far field. Each particle evolves and convects in the far field, then is split (every *N* time steps) to simulate the diffusion effect. This completes the calculation in the current time step, and the whole process repeats for the next time step.

D. Tip Vortex Core Parameter Identification

The identification of the tip vortex core parameters, namely size and location, is adopted from the procedure presented in Ref. 16. In the experiment, an approximate location of the tip vortex at some distance behind the trailing edge was measured using a vortex meter. Then a laser velocimeter was used to measure swirl velocity across the vortex core in the spanwise direction. The vortex core size reported is the distance between the locations of the maximum and minimum swirl velocity across the core. The precise location of the core was determined to be the mid-point between the minimum and maximum swirl velocity.

Similar methodologies are employed for the computational results. To identify the vortex core parameters inside a RANS domain, the approximate location of the tip vortex core is determined by searching for the maximum amplitude of vorticity in a given plane behind the trailing edge. Once this is known, the swirl velocity across the vortex core is calculated by linear interpolation, and then the core size and precise location of the core are calculated in the same manner as in the experiment.

A slightly different procedure is used for

identifying the vortex core parameters for the PVTM domain, since the PVTM analysis does not calculate the velocity field directly. At the desired distance behind the trailing edge, a properly located velocity measurement plane is created to record the induced velocity from the vortex particle field. These are shown in Figure 6 for 1, 2, 4, and 6 chords behind the airfoil. The induced velocity field from the vortex particles is calculated in each measurement plane, similar to particle image velocimetry measurements in an experiment. The velocity fields are processed into vorticity with the strength vector perpendicular to the measurement plane. The vorticity field is searched to find the location of the maximum vorticity, to obtain the location of the vortex core. The swirl velocity can be extracted directly from the measurement plane, to obtain the core size in the same way as for the measurement and RANS-calculated velocity field. For the PVTM vortex parameters, 200 time steps are averaged to obtain the vortex parameters. This is necessary because the induced velocities from the particles are highly dependent on the proximity of the particle to the point where the velocity is being calculated. Averaging smoothes out this nonlinearity to obtain a more consistent result.

E. Stability Enhancement Procedure for Particle Vortex Method

One of the stability conditions cited in Ref. 17 was that the flow field must be divergence free at all time. This requires the vorticity field to be uniformly distributed and align itself properly. Several modifications to the induced velocity and stretching term calculations are made to achieve this goal as shown below. The induced velocity equation is changed from Eq. (6a) to (6b). An attraction term (2nd term) is added to counteract the tendency of the particles to slowly drift apart in the simulation, which helps the vortex core to maintain its compactness and coherence.

$$u(x) = \sum_i -\frac{1}{4\pi}\frac{(x-y_i)\times\beta_i}{\left(|x-y_i|^2+\delta^2\right)^{3/2}} \tag{6a}$$

$$u(x) = \sum_i -\frac{1}{4\pi}\left(\frac{(x-y_i)\times\beta_i + \eta_1(x-y_i)|(x-y_i)\times\beta_i|}{\left(|x-y_i|^2+\delta^2\right)^{3/2}}\right) \tag{6b}$$

The stretching term is modified from Eq. (7a) to (7b) to help align the strength vector of each vortex particle based on the strength of the surrounding particle field. In effect, this is analogous to the Particle Strength Exchange (PSE) method[20].

$$\beta^P \bullet \nabla u = \sum_i \frac{1}{4\pi}\left[\frac{\beta^P\times\beta_i}{\left(|x-y_i|^2+\delta^2\right)^{3/2}} + \frac{3\left(\beta^P\cdot(x^P-y_i)\times\beta_i\right)(x-y_i)}{\left(|x-y_i|^2+\delta^2\right)^{5/2}}\right] \tag{7a}$$

$$\beta^P \bullet \nabla u = \sum_i \frac{1}{4\pi}\left[\eta_2|\beta_i|\frac{\left(\beta^P\times\beta_i\right)\times\beta^P}{\left(|x^P-x_i|^2+\delta^2\right)^{3/2}}\right] \tag{7b}$$

The coefficients η_1 and η_2 control the overall stability of the PVTM calculation. They depend on a number of parameters including time step size (*dt*), and in this particular case they are chosen to be 0.005 and 5, respectively.

IV. Results

A. Pressure Distribution

Obtaining the pressure distribution around the airfoil from the RANS calculation is straightforward. The test data includes pressure distributions at several span stations along the wing. The first thing to be verified is the

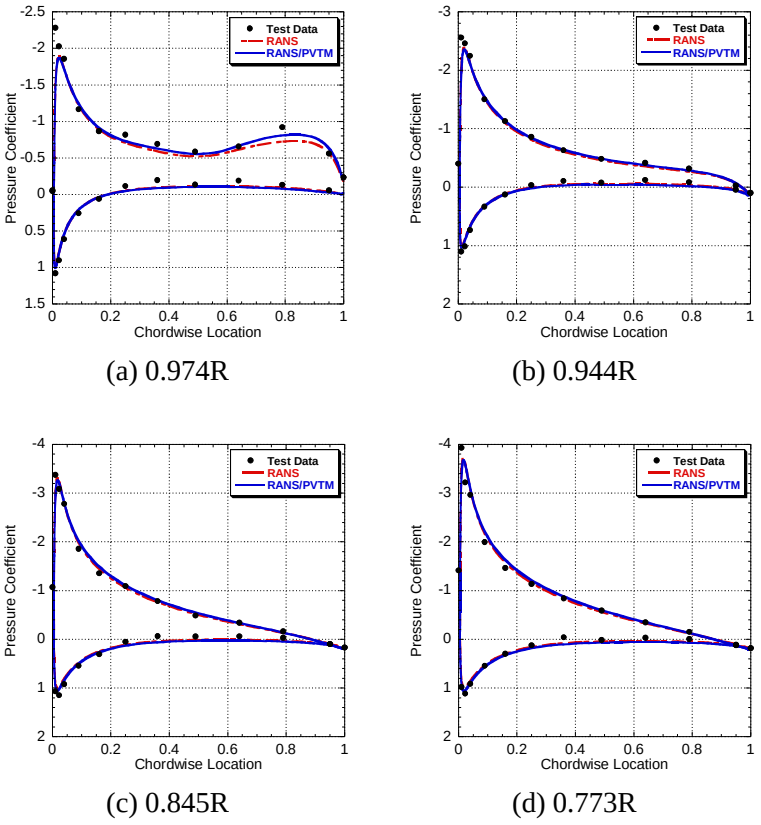

Figure 7. Airfoil surface pressure distributions near the wing tip.

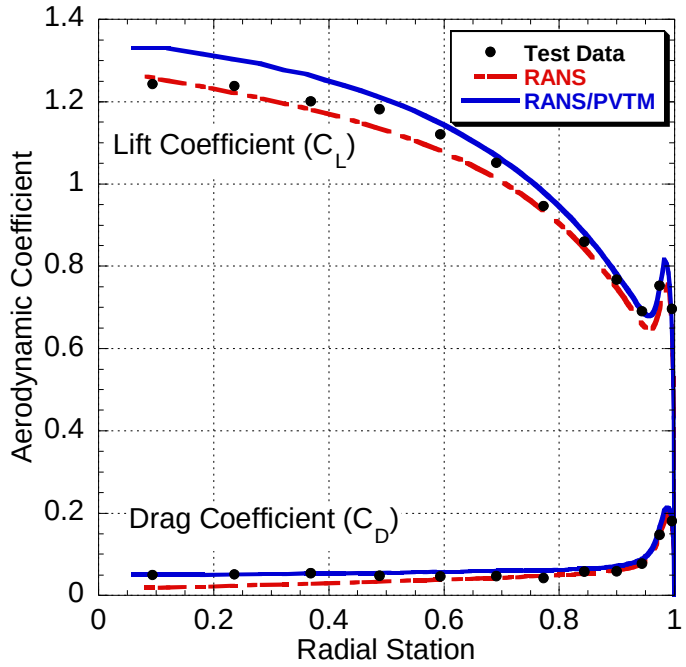

Figure 8. Lift and drag coefficients along wing span derived from surface pressures.

prediction of the pressure field around the airfoil which is highly affected by the near field wake as well as the far field wake. For the coupled method, the influence of the trailed vortex must be correctly accounted for inside the RANS domain for accurate prediction of the pressure field on the airfoil surface.

Surface pressures for four radial stations near the wing tip are shown in Figure 7. The surface pressures are visibly affected by the tip vortex outboard of 0.845, but inboard of 0.845, the pressure distributions are the same. The plots show that the hybrid RANS/PVTM method captures the variation in surface pressure at least as well as the baseline RANS calculation. For the outermost radial station, the result from the hybrid RANS/PVTM calculation is closer to the test data near the trailing edge (0.8c). The surface pressures are integrated to obtain lift and drag along the wing span, shown in Figure 8. The spanwise variation in lift and drag due to the tip vortex is well captured for both the RANS and hybrid RANS/PVTM calculations. These results show that the interchange of vorticity and velocity between the near-body RANS grid and the off-body PVTM domain is properly implemented.

B. Vorticity Sources

Using the near-body RANS grid can yield several advantages over some simplified methods such as lifting line theory or vortex panel method. The RANS calculations provide much more detailed flow field information such as pressure, loading, and shape of the tip vortex, than other methods. This is shown with the different profiles of the vorticity in the region of the tip vortex at the interface between the RANS and PVTM domains for the square and rounded tip wings in Figure 9. The vortex sheet being trailed behind the wing and the tip vortex are visible, and the different character of the tip vortex is evident between the two tip geometries. For the square tip wing, the tip vortex is formed from smaller vortices being shed from the upper and lower edges, while for the round tip wing, a single compact tip vortex is shed from the tip. This sort of detail is not captured unless a viscous, 3D RANS simulation is used in the near-body region.

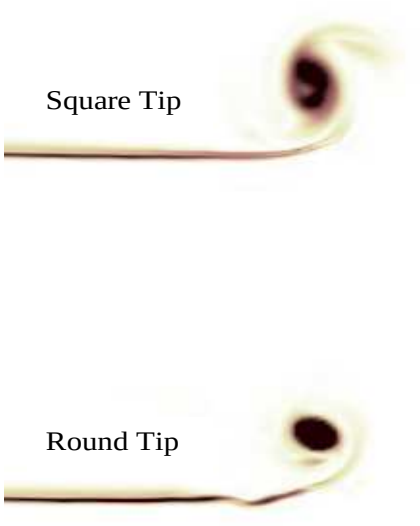

Figure 9. Vorticity distribution in vortex sheet and tip vortex for square and round tip airfoils.

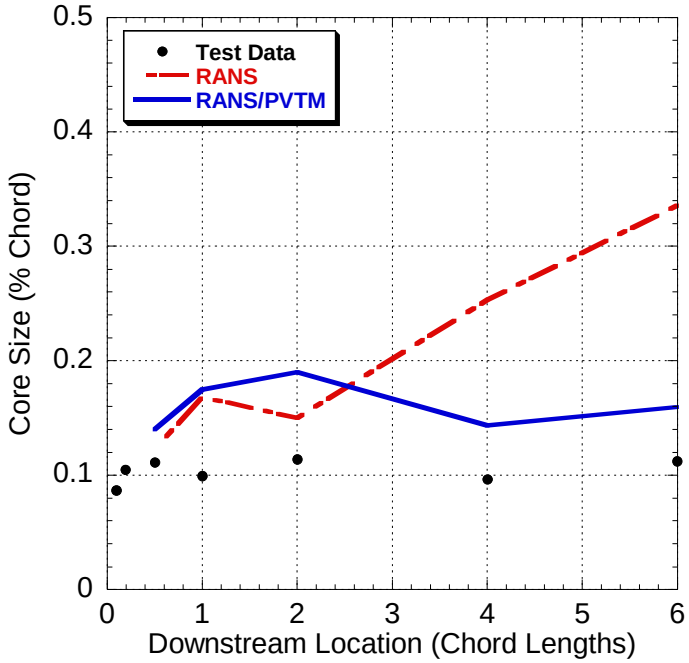

Figure 10. Vortex core size downstream of the wing.

C. Tip Vortex Geometry

The next comparison verifies the vortex geometry, namely size and location, of the tip vortex. Figure 10 shows the vortex core size as a function of downstream location and Figure 11 shows its location. Both the RANS and hybrid RANS/PVTM calculations show an offset in core size near the trailing edge. Downstream, however, the core size steadily increases in the RANS calculation, while the hybrid calculation maintains a nearly constant core size which compares well with the test data.

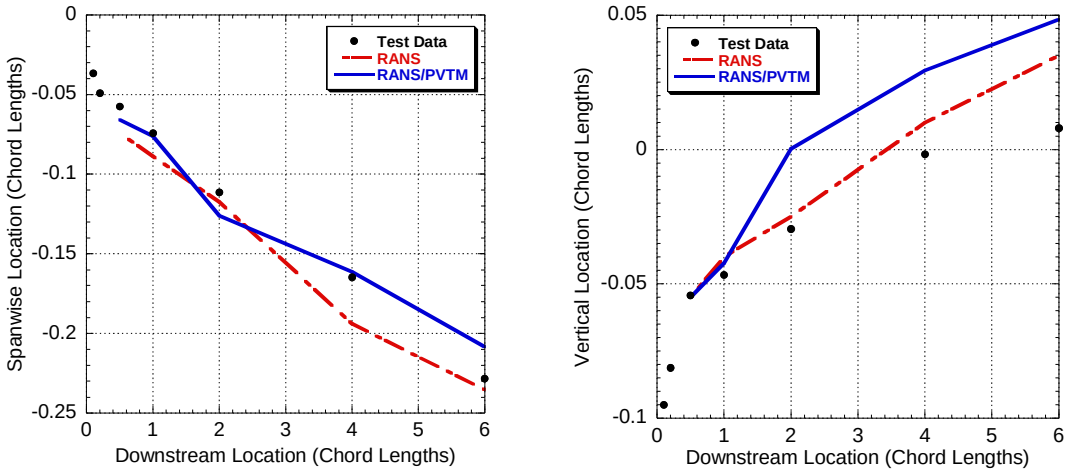

(a) Spanwise location (b) Vertical location

Figure 11. Spanwise and vertical locations of tip vortex downstream of the wing.

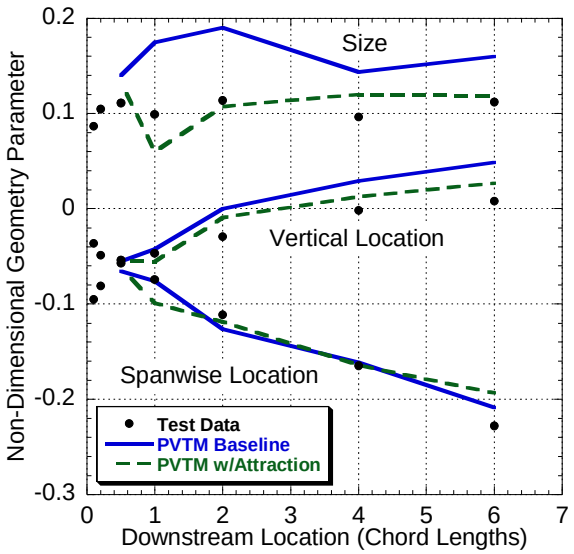

Figure 12. Tip vortex geometry calculated by the RANS/PVTM method with and without additional attraction term.

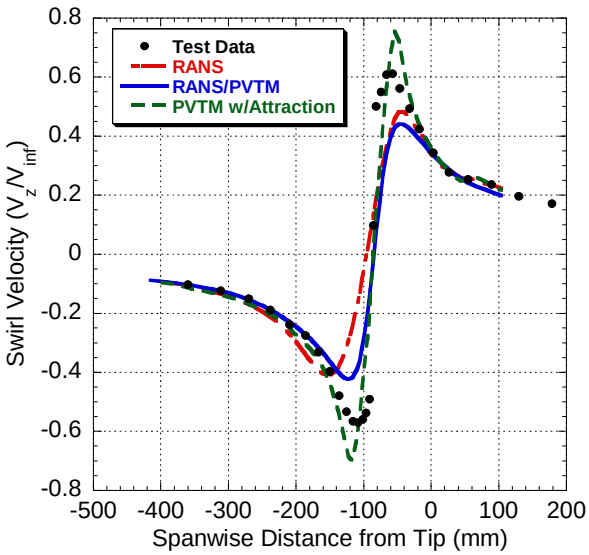

Figure 13. Swirl velocity profile across tip vortex four chords behind trailing edge.

The location of the tip vortex is shown in Figure 11. The variation in spanwise location is captured well in both the RANS and hybrid RANS/PVTM methods. The correlation of vertical location is not as good, but the magnitude of the variation is also only half that of the spanwise location, making the differences appear larger. The vortex does gradually drift upward like the experiment for both cases. The vortex attraction term can be used to improve the correlation. The PVTM results with and without the attraction term are compared to the test data in Figure 12. With the attraction term, the offset in core size is removed such that the calculated core size matches the experimental data very closely. The vertical location of the tip vortex is also improved.

D. Velocity Profiles

Velocity profiles at four and six chords behind the airfoil are shown in Figure 13 and Figure 14, respectively. For both the RANS and hybrid RANS/PVTM calculations, the peak velocities are under-predicted. At 6 chords, the numerical diffusion in the pure RANS calculation is evident while the hybrid method maintains a stable and compact core size. The attraction term results in a much sharper gradient through the core and hence a smaller tip vortex. From these figures, it is not as obvious what the core size is as in Figure 12, for example, but the general trend can be established. It is clear that the attraction term causes the peak velocity to be over-predicted, so careful selection of the attraction parameters is important.

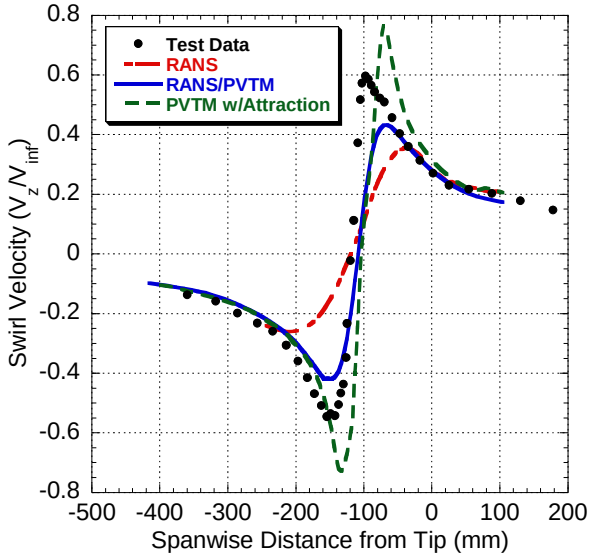

Figure 14. Swirl velocity profile in tip vortex six chords behind trailing edge.

Finally, the effects of viscous diffusion are shown in Figure 15. The three calculations are the baseline PVTM, PVTM with the attraction term, and PVTM with both the attraction term and viscous diffusion. It is clear that the diffusion makes no difference to the resolution of the plot. This is not entirely unexpected as 6 chords is a very young wake age and the effects of real viscosity in the tip vortex should not be evident until much farther downstream.

V. Conclusions

A hybrid Reynolds-Averaged Navier-Stokes and Particle-based Vorticity Transport Method solution

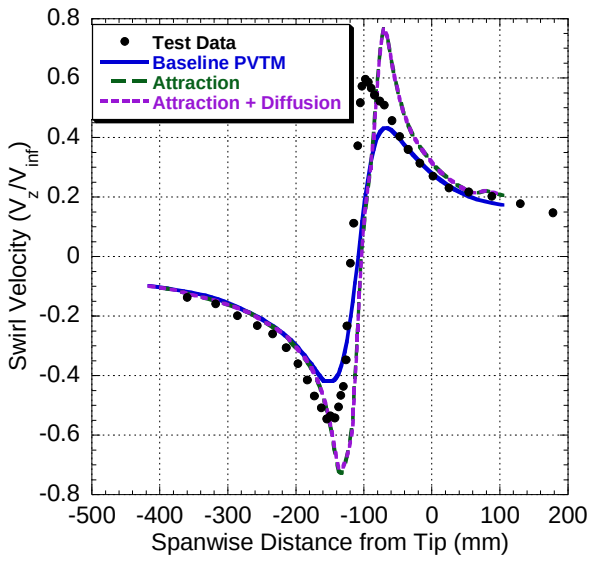

Figure 15. Velocity profile in tip vortex for PVTM calculation six chords behind the trailing edge, showing influence of attraction term and viscous diffusion.

methodology has been presented and validated against test data for a fixed wing in a wind tunnel. Based on the results observed in this study, the following conclusions are offered.

The combination of vortex shedding from the near body domain into the PVTM domain and the field velocity method for communicating the influence of the far wake on the near body domain is an effective coupling methodology. The three-dimensional effects of the wing tip were properly modeled in the near body domain. Correlation between calculated lift and drag coefficients and measured data was satisfactory.

The hybrid method resulted in less numerical dissipation of the tip vortex than the baseline RANS calculation, which showed significant diffusion by 4-6 chords wake age. For the hybrid method, the core size was initially larger than in the experiment, but maintained nearly constant size, similar to the test data. The location of the vortex was satisfactorily captured by both the pure RANS and the hybrid method.

An added attraction term improved correlation with test data by reducing the size of the vortex core. Viscous diffusion did not have an effect on the results for wake ages up to 6 chords.

Acknowledgments

Phuriwat Anusonti-Inthra is supported under NASA Contract NAS1-2117, Task Order NNL04AA96T (Rotorcraft Aeromechanics) with Dr. Mark W. Nixon (Army Research Laboratory) as a technical monitor, and NASA Contract NNL07AA32C with Dr. Douglas Nark as a technical monitor.

References

[1]Chow, J., Zilliac, G, and Bradshaw, P., "Turbulence Measurements in the Near Field of a Wingtip Vortex," *NASA TM 110418*, 1997

[2]Chigier, N.A. and Corsiglia, V.R., "Tip Vortices – Velocity Distributions," *NASA TM X-62087*, 1971

[3]Campbell, S.D. et al., "Wake Vortex Field Measurement Program at Memphis, TN: Data Guide", *NASA CR-201690*, MIT Lincoln Laboratory, Lexington, MA, 1997

[4]Crow,S.C. and Bates, E.R., "Lifespan of trailing vortices in a turbulent atmosphere," *J. of Aircraft*, Vol. 13, pp 476, 1976

[5]Ortega, J.M., "Stability Characteristics of Counter-Rotating Vortex-Pairs in the Wakes of Triangular-Flapped Airfoils," Ph.D. Dissertation, Dept. of the Chemical Engineering, U. of California, Berkley, 2001

[6]Chevalier, H., "Flight Test Studies of the Formation and Dissipation of Trailing Vortices," *J. of Aircraft*, Vol. 10, No.1, pp. 14-18, 1973

[7]Crow, S. C., "Stability Theory for a Pair of Trailing Vortices," *AIAA Journal*, Vol. 8, No. 12, pp. 2172–2179, 1970

[8]Devenport, W.J., Vogel, C.M., and Zsoldos, J.S., "Flow Structure Produced by the Interaction and Merger of a Pair of Co-Rotating Wing-Tip Vortices," *J. of Fluid Mechanics*, Vol. 394, pp 356-377, 1999

[9]Rossow, V. J., "Inviscid modeling of aircraft trailing vortices," NASA SP409. 1977

[10]Smith, S. C. and Kroo, I. M., "Induced Drag Computations on Wings with Accurately Modeled Wakes," *Journal of Aircraft*, Vol. 34, No. 2, pp. 253–255,1997

[11]Rossow, V., "Classical Wing Theory and the Downward Velocity of Vortex Wakes," *J. of Aircraft*, Vol. 43, No. 2, pp. 381-385, 2006

[12]Stumpf, E., "Study of Four-Vortex Aircraft Wakes and Layout of Corresponding Aircraft Configurations," *J. of Aircraft*, Vol. 42, No. 3, pp.722-730, 2005

[13]Chatelain, P. et al.: Billion vortex particle direct numerical simulations of aircraft wakes, *Computer Methods in Applied Mechanics and Engineering*, Vol. 197,pp. 1296-1304, 2008

[14]Anusonti-Inthra, P., "Development of Rotorcraft Wake Capturing Methodology Using Fully Coupled CFD and Particle Vortex Transport Method," *Proceedings of the 62nd AHS Annual Forum*, Phoenix, AZ, 2006

[15]Sitaraman, J., "CFD Based Unsteady Aerodynamic Modeling for Rotor Aeroelastic Analysis", PhD. Dissertation, Dept. of Aerospace Engineering, University of Maryland, 2003
[16]McAlister, K. and Takahashi, R.K., "NACA0015 Wing Pressure and Trailing Vortex Measurements," *NASA-TP-3151*, 1991
[17]Winckelmans, G. S., "Topics in Vortex Methods For the Computation of Three- and Two-dimensional incompressible unsteady flows," PhD. Dissertation, California Institute of Technology, 1989
[18]Subramaniam, S., "A New Mesh-Free Vortex Method," Ph.D. Dissertation, Florida State University, 1996
[19]Gharakhani, A., "A Higher Order Vorticity Redistribution Method for 3-D Diffusion in Free Space," *Sandia Report*, Sandia National Laboratories, SAND2000-2505, 2000
[20]Cottet, G.H. and Koumoutsakos, P., "Vortex Methods –Theory and Practice," Cambridge University Press, New York, 2000.